Variational Graphical Quantum Error Correction Codes: adjustable codes from topological insights

Yuguo Shao,[1,2] Fuchuan Wei,[1,2] Zhaohui Wei,[1,3] and Zhengwei Liu[1,2,3,*]

[1]*Yau Mathematical Sciences Center, Tsinghua University, Beijing 100084, China*
[2]*Department of Mathematics, Tsinghua University, Beijing 100084, China*
[3]*Yanqi Lake Beijing Institute of Mathematical Sciences and Applications, Beijing 100407, China*

In this paper, we leverage the insights from Quon, a picture language for quantum information, to develop a new class of quantum error-correcting codes termed Variational Graphical Quantum Error Correction (VGQEC) codes. The VGQEC codes feature adjustable configuration parameters that play a pivotal role in determining the error-correcting capability of the codes. This key feature offers remarkable flexibility in customizing high-quality quantum error-correcting codes for various noise models. For instance, we will present a specific VGQEC code that exhibits a seamless transition of parameters, enabling the smooth transformation of the code from the five-qubit repetition code to the [[5,1,3]] code, and furthermore, the new VGQEC code has a better performance than the above two well-known codes under certain noise models. Meanwhile, we also propose a general physical scheme to implement and optimize VGQEC codes in realistic quantum devices. Lastly, we apply our approach to amplitude damping noise, and by numerical calculations, we discover an unexpected novel three-qubit code that can effectively mitigate the noise.

I. INTRODUCTION

In recent years, the field of quantum computing has undergone substantial growth and demonstrated great potential in effectively solving certain hard computational problems [1–7]. However, physical implementations of quantum information processing tasks are unavoidably subject to noise, which could eradicate useful quantum information. To solve this problem, it is essential to implement active quantum error correction (QEC) to mitigate errors that occur dynamically during the storage and the processing of quantum information [8–11]. In a typical QEC scheme, quantum information is protected by storing it in QEC codes through an *encoding* procedure. A common approach to designing QEC codes involves utilizing the Pauli framework to tailor codes for generic noise acting on a small but unknown subset of qubits [12–23]. However, in practical devices, quantum information is subject to hardware-specific quantum noise processes, which differ significantly across various physical platforms [24–26]. Furthermore, the error model might change over time, or part of the qubits in a real-world device might be more prone to errors than others. Therefore, the general-purpose codes described above may not be optimal for the specific noise characteristics of a given device [27].

Nowadays, many attempts have been directed toward the development of noise-tailored codes. For instance, the 4-qubit code [27], tailored for mitigating amplitude damping noise, as well as the cat-codes [28, 29] and binomial codes [30], both devised to safeguard information stored in boson modes. However, the construction of noise-tailored codes for arbitrary noise poses significant difficulty. Therefore, adaptive methodologies for search-

ing codes have been explored. A common approach is to reformulate the search for effective error correction schemes as an optimization problem [31–37]. Through this approach, noise-tailored codes can be obtained by numerically solving the optimization problem under specific noise. These methods usually require characterizing the noise model, and the optimization problem's scale usually grows exponentially with the number of qubits, making them impractical for large-scale quantum systems. With the popularity of machine learning, a series of learning-based approaches for discovering noise-tailored codes have been proposed [38–44]. These methods generally rely on experimentally accessible data and interactions with the quantum device to automatically construct noise-tailored codes, thus avoiding the exponential cost of computing quantum processes classically. However, in the above schemes, the target code is usually learned from scratch without leveraging the prior knowledge from general-purpose codes. In this work, we propose a new learning-based strategy that circumvents the need to learn codes from scratch, but instead modifies established general-purpose codes to accommodate various noise models.

Recently, a mathematical picture language [45] called *Quon 3D language* has been developed to study quantum information [46]. Specifically for quantum error correction, it provides a versatile graphical methodology for investigating codes [47]. It has been demonstrated that the error correction capabilities of codes can be visualized through their Quon graphs. This inspired us to design a variable graphical framework, which enables codes to optimize for specific noise models by adjusting the Quon graph structure. We propose a novel scheme for this purpose, called *Variational Graphical Quantum Error Correction (VGQEC) codes*. The VGQEC codes are characterized by multiple adjustable parameters, enabling the modification of the Quon diagram structure by manipulating these parameters. For the practical-

---

ity of the VGQEC code, we propose a hybrid quantum-classical scheme for parameter optimization of VGQEC under the variational quantum circuit framework. We numerical tested the scheme under amplitude damping noise and thermal relaxation process, and found that the VGQEC codes effectively adapt to the noise with significant performance improvement. In particular, for amplitude damping noise, our numerical results identified a novel 3-qubit code that effectively mitigates the effect of noise. To the best of our knowledge, this is the smallest code for amplitude damping noise.

II. PRELIMINARIES

The main idea of quantum error correction is to encode logical qubits into noisy physical qubits. The general mathematical formalism of quantum error correction is summarized as follows. Let $\mathcal{H}$ be the two-dimensional Hilbert space of the single qubit. In general, the k-qubit quantum information that needs to be protected can be represented as a density operator ρ in $\mathcal{L}(\mathcal{H}^{\otimes k})$. To realize the error correction process, k qubits of logical quantum information in $\mathcal{L}(\mathcal{H}^{\otimes k})$ are encoded via an encoding map $\mathcal{E} : \mathcal{L}(\mathcal{H}^{\otimes k}) \to \mathcal{L}(\mathcal{H}^{\otimes n})$ into n physical qubits in $\mathcal{L}(\mathcal{H}^{\otimes n})$. In this context, the number of physical qubits n is greater than logical qubits k, resulting in the addition of redundant information to the encoded state $\mathcal{E}(\rho)$. Subsequently, the n physical qubits are subjected to a noise channel $\mathcal{N} : \mathcal{L}(\mathcal{H}^{\otimes n}) \to \mathcal{L}(\mathcal{H}^{\otimes n})$. To mitigate the effects of the noise channel, the recovery map $\mathcal{R} : \mathcal{L}(\mathcal{H}^{\otimes n}) \to \mathcal{L}(\mathcal{H}^{\otimes k})$ is employed to recover information by extracting redundant data from the encoded quantum states. Quantum error correction protects information against noise by making the process sequence approximate the identity channel, $\mathcal{R} \circ \mathcal{N} \circ \mathcal{E} \approx \mathcal{I}$.

There are many metrics quantifying the disparity between $\mathcal{R} \circ \mathcal{N} \circ \mathcal{E}$ and $\mathcal{I}$ based on *fidelity* and *distance* [1, 48]. Two common candidate are the *Average Entanglement Fidelity* [49] and *Channel fidelity* [37]. Average entanglement fidelity is defined for a channel $\mathcal{M}$ and an ensemble $E = \{\rho_i, p_i\}$ of states ρ_i with probabilities p_i as

$$\overline{F_e}(E, \mathcal{M}) \equiv \sum_i p_i F_e(\rho_i, \mathcal{M}) = \sum_{i,j} p_i |\operatorname{Tr}\{\rho_i M_j\}|^2 \quad (1)$$

where $\{M_j\}$ are the Kraus elements of the channel $\mathcal{M}$. In the context where the ensemble E is selected as the completely mixed state $E = \{I/d, 1\}$, with d representing the dimension of Hilbert space, the average entanglement fidelity takes the value of channel fidelity:

$$F_C(\mathcal{M}) = \frac{1}{d^2} \sum_j |\operatorname{Tr} M_j|^2. \quad (2)$$

While choosing $\mathcal{M} = \mathcal{R} \circ \mathcal{N} \circ \mathcal{E}$, the above fidelity metrics measure the effectiveness of the code in protecting quantum information against noise.

To better protect information, the encoding and recovery map should be chosen to match the features of the noise channel. Solving the following approximate error correction condition is a potential way to design codes tailored to specific noise models $\mathcal{N}$. For a code with encoding map $\mathcal{E}$, if there exists a recovery map $\mathcal{R}$ such that the worst-case entanglement fidelity $\min_\rho F_e(\rho, \mathcal{M})$ for $\mathcal{M} = \mathcal{R} \circ \mathcal{N} \circ \mathcal{E}$ is greater than $1 - \varepsilon$, then the code is said to be ε-correlatable for $\mathcal{N}$. Ref. [50] propose a sufficient and necessary condition for approximate quantum error correction: a code with encoding map $\mathcal{E}$ is ε-correlatable for $\mathcal{N}(\rho) = \sum_i E_i \rho E_i^\dagger$ if and only if

$$P_c E_i^\dagger E_j P_c = \lambda_{ij} P_c + P_c B_{ij} P_c, \quad (3)$$

where P_c is the projector on the code space $\operatorname{Im}(\mathcal{E})$, $\{\lambda_{ij}\}$ is a non-negative Hermitian matrix with trace one, B_{ij} is a Hermitian matrix, and the Bures distance [51] between two channels $\Lambda(\rho) = \sum_{ij} \operatorname{Tr}\{\rho\} |i\rangle\langle j|$ and $(\Lambda + \mathcal{B})(\rho) = \Lambda(\rho) + \sum_{ij} \operatorname{Tr}\{\rho B_{ij}\} |i\rangle\langle j|$ satisfies

$$d(\Lambda, \Lambda + \mathcal{B}) \leq \varepsilon. \quad (4)$$

When $B_{ij} = 0$ for all i, j, this condition reduces to the perfect error correction condition (known as the *Knill-Laflamme condition*) [52]. In principle, constructing error-tailored codes is to find the solution P_c of the equation (3). However, this equation is difficult to solve in practice, and the solution may not be unique.

On the other hand, recovery maps are usually composed of manually designed syndrome measurements for detecting errors and unitary operators for correcting errors [1]. Alternatively, the recovery maps can be obtained by solving optimization. Under a given input state ensemble and noise model, the recovery map can be chosen to maximize the average entanglement fidelity (1) by solving a semi-definite program (SDP) [53]. Specifically, by setting the input state ensemble as the encoded completely mixed state $\mathcal{E}(I/d)$, the output of the SDP $\mathcal{R}_{opt}$ is optimum for the given encoding map $\mathcal{E}$ and noise channel $\mathcal{N}$ in the sense of channel fidelity (2):

$$\mathcal{R}_{opt} = \arg\max_{\mathcal{R}} F_C(\mathcal{R} \circ \mathcal{N} \circ \mathcal{E}). \quad (5)$$

III. VARIATIONAL GRAPHICAL CODES

Quon is a 3D topological language specifically designed for quantum information [46]. For quantum error correction, the Quon language provides a general method for studying codes and a new pictorial method to construct codes [47]. Our method improves codes by incorporating customizable parameters into their Quon graphs. More precisely, for any code, parameters can be embedded within its Quon graph, enabling dynamic modifications to its graph structure through parameter manipulation. Consequently, a parameterized code can be derived from
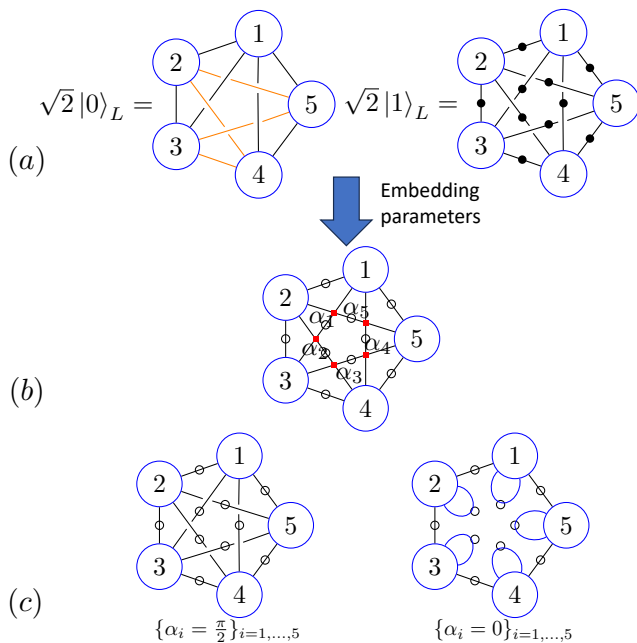
Figure 1. (a) Quon graphs of the logical states of $[[5,1,3]]$ code are constructed from quantized graph K_5 whose five vertices are physical qubits. (b) An example of five-qubit VGQEC code. There are five variable parameters $\{\alpha_i\}_{i=1,\ldots,5}$ added to crossings. The $\circ$ symbol represents the positions where charges can potentially be added. The Quon graphs represent logic $|0\rangle_L$ when no charge is added, and represent logic $|1\rangle_L$ when all charges are added. (c) When the parameters α_i are all set to $\frac{\pi}{2}$, the discs are connected by strings to each other, resulting in the $[[5,1,3]]$ code. When $\{\alpha_i = 0\}_{i=1,\ldots,5}$, five crossings are removed, the modification makes the code become a five-qubit repetition code in the X-basis.
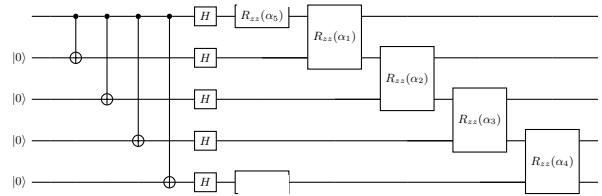

Figure 2. The encoding circuit for the VGQEC code in Fig. 1(b). The $R_{ZZ}(x)$ gates represent the two-qubit Pauli rotation $e^{-i\frac{x}{2}Z\otimes Z}$, and the half-open $R_{ZZ}(x)$ gate is applied to the first and fifth qubits.

this graph, allowing adaptation to various noise environments through parameter optimization. We call the parameterized codes derived from this manner as VGQEC.

For instance, the logical state of $[[5,1,3]]$ code can be visualized as a fully connected diagram K_5 shown in Fig. 1(a). The alignment of this representation with the $[[5,1,3]]$ code can be verified through stabilizers. Stabilizers of the code can be represented by cycles with even-length in its Quon graph. More details are elaborated in Appendix B.

One optional simple modification is to substitute the hidden parameters of the crossings with variable parameters $\{\alpha_i\}_{i=1,\ldots,5}$, as shown in Fig. 1(b). Such a VGQEC code effectively bridges the gap between the five-qubit repetition code and the $[[5,1,3]]$ code. Specifically, setting the parameters $\alpha_i = \frac{\pi}{2}$ for $i = 1,\ldots,5$ yields the five-qubit $[[5,1,3]]$ code, as illustrated in Fig. 1(c). Conversely, assigning 0 to the parameters $\{\alpha_i\}$, the logical $|0\rangle_L$ and $|1\rangle_L$ are $|{+}{+}{+}{+}{+}\rangle$ and $|{-}{-}{-}{-}{-}\rangle$, respectively. At this point, the VGQEC code corresponds to the five-qubit repetition code on the basis $|+\rangle, |-\rangle$. Moreover, from the Quon graph of the VGQEC code, we can derive its encoding circuit, as shown in Fig. 2. By setting

$\alpha_i = \frac{\pi}{2}$, we obtain a new encoding circuit for the $[[5,1,3]]$ code.

To demonstrate the potential of this VGQEC, a specific noise evolution process was examined, and the parameters of the VGQEC were optimized to adapt the noise at each moment of the process, as detailed in Appendix C. Within this process, the noise comprises a variable Pauli error channel $\mathcal{N}_1^\eta$ with parameters η, a fixed correlated error channel $\mathcal{N}_2$, and a fixed amplitude damping channel $\mathcal{N}_3$. With an increase in η, the variable Pauli error channel $\mathcal{N}_1^\eta$ transforms from a dephasing to a depolarizing channel. In the ideal case, assuming all the information about the noise is available, the optimal recovery map (5) obtained by SDP can be employed, thereby permitting an assessment that focuses solely on the performance of the encoding scheme. As shown in Fig. 3, the optimized VGQEC initially approximates the five-qubit repetition code when η is small. As the noise evolves, the VGQEC is eventually transformed into the $[[5,1,3]]$ code. Throughout this noise evolution, the VGQEC consistently demonstrates superior information protection compared to both the repetition code and the $[[5,1,3]]$ code, highlighting its advantages in general noise scenarios. The automatic adaptability to diverse noise environments of VGQEC derives partly from its ability to flexibly switch between multiple codes based on noise characteristics. By leveraging the strengths of multiple codes, the VGQEC can achieve superior performance over them. Besides, the interpolating process between these codes yields new codes, further enhancing the potential of VGQEC.

IV. HYBRID QUANTUM-CLASSICAL SCHEME FOR OPTIMIZING VGQEC

Based on graphical insights, we have developed VGQEC codes. However, in general, compiling their encoding maps into quantum circuits presents a significant challenge, especially for VGQEC codes with complex structures. Moreover, employing optimal recovery maps [53] or Petz recovery maps [54, 55] necessitates comprehensive characterization of the noise model in quantum devices, compilation of these maps into circuits, as well as substantial computational resources. These com-
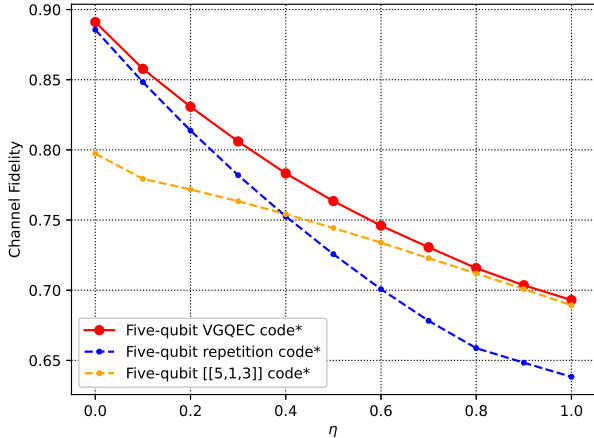
Figure 3. Interpolation from the five-qubit repetition code to the $[[5, 1, 3]]$ code. The horizontal axis η denotes the evolution of noise, and the vertical axis is the channel fidelity (2). During the noise evolution detailed in Appendix C, the optimized VGQEC designed from the Quou graph in Fig. 1(b) gradually transitions from the repetition code to the $[[5, 1, 3]]$ code. The symbol $*$ represents the recovery map is the optimal recovery map (5) obtained by SDP optimization.

Figure 4. The performances of optimized VGQEC codes and original codes under amplitude damping channel.

plexities render the application of such recovery maps impractical in real-world scenarios.

To address these challenges, we propose a hybrid quantum-classical scheme for implementing VGQEC using variational quantum circuits, suitable for execution on NISQ devices [56]. Firstly, we design a class of VGQEC codes, whose Quon graphs are constructed by gluing a specially designed graphical structure to the physical qubits of the original code. For this class of VGQEC codes, we can efficiently compile their encoding maps into variational quantum circuits. In terms of the recovery map, we employ the combination of variational quantum circuits and the recovery maps of the original code. This recovery map can not only implement the recovery map of the original code but also has the flexibility to be further optimized. To optimize the parameters within the VGQEC codes and their associated recovery circuits, we employ the average entanglement fidelity [49] as the objective function and use a variational quantum algorithm inspired by [42] to maximize the metric. Finally, the encoding and recovery circuits are directly accessible after optimization. The details can be found in Appendix D.

We numerically investigate the performance of the scheme. Our investigation focuses on three-qubit and five-qubit VGQEC codes, derived from the three-qubit repetition code and the $[[5, 1, 3]]$ code, respectively. We examined scenarios involving amplitude damping noise and thermal relaxation process. In the amplitude damping case, we assume that the noise intensity is the same for all qubits, while in the thermal relaxation process,
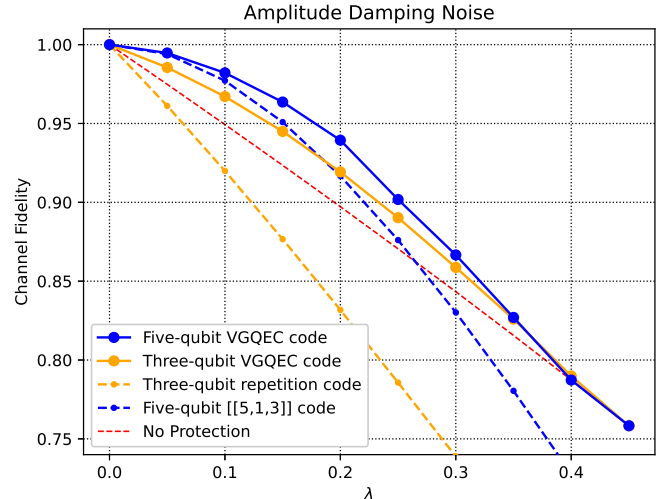
the noise intensity varies from qubit to qubit. More details about numerical simulations can be found in Appendix E. To avoid ambiguity, we clarify that the five-qubit VGQEC in this section is different from the simple structure in Fig. 1.

As shown in Fig. 4, the three-qubit cannot effectively protect information under amplitude damping channels compared to the scenario with no code protection. However, the three-qubit VGQEC code, derived from the repetition code, significantly increases the channel fidelity compared to the original code. Surprisingly, the three-qubit VGQEC outperforms the five-qubit $[[5, 1, 3]]$ code when the damping parameter $\gamma \geq 0.2$. Similarly, for the five-qubit VGQEC code, the scheme can also improve the performance of the five-qubit $[[5, 1, 3]]$ code. Compared with the three-qubit case, the longer VGQEC code utilizes more redundant information to obtain higher channel fidelity.

By analyzing the optimized results, we find that the optimized three-qubit VGQEC has the following codewords:

$$|0\rangle_L = \frac{1}{\sqrt{2}}(|000\rangle + i\,|110\rangle),$$

$$|1\rangle_L = \frac{1}{\sqrt{2}}(i\,|001\rangle + |111\rangle).$$

This code protects information from amplitude damping noise well, and hasn't been reported in other works, as far as we know.

As reported in [57], the publicly-available coherence time data of the *IBMQ-LIMA* (5-qubit) device is shown in Table I (It is worth noting that IBM devices are calibrated almost every day and error reports are updated after each calibration cycle). From the data table, it is clear that the noise intensity varies from qubit to qubit.

Q_4 has the shortest coherence time, meaning that Q_4 suffers the most intense noise. Among the five qubits examined, qubit Q_0 demonstrates the highest quality based on numerical results, while it exhibits the highest channel fidelity.

Qubit	Q_0	Q_1	Q_2	Q_3	Q_4
T_1	97.51 μ s	127.61 μ s	92.68 μ s	79.36 μ s	19.76 μ s
T_2	178.3 μ s	109.28 μ s	120.95 μ s	35.71 μ s	19.4 μ s

Table I. Coherence time data of IBMQ-LIMA device. The five qubits in the device are labeled by $Q_0, \ldots, Q_4$.

We consider a thermal relaxation process with duration t occurring in the five-qubit quantum system, which is characterized by the coherence time shown in Table I. The description of the thermal relaxation process can be found in Appendix E 2. The [[5, 1, 3]] code is designed to correct arbitrary errors on individual qubits. Therefore, when the qubits have different qualities, the symmetrically designed [[5, 1, 3]] code is difficult to perform well. As shown in Fig. 5, when $t \geq 2.5$, the channel with original [[5, 1, 3]] code protection has a lower channel fidelity than unprotected high-quality single qubit channel (Q_0). This indicates that the [[5, 1, 3]] code is not suitable for the asymmetric noise setting. However, the five-qubit VGQEC code shows a significant performance improvement compared to the original [[5, 1, 3]] code, and the performance is close to the numerically-optimized results obtained by the iterated convex optimization method [35]. Our scheme can effectively capitalize on the different qualities of qubits to optimize the VGQEC code, enhancing the performance of the code under asymmetric noise settings.

V. DISCUSSION

In this work, we introduce a scheme called VGQEC to make codes trainable. We represent the given stabilizer code as a Quon graph, and the properties of the Quon graph allow us to add parameters to the graph. The adjustment of parameters realizes the change in the structure of the Quon diagram. This also allows us to transform from one stabilizer code to another. Since the Quon diagram structure of code is related to its error correction capability, this allows us to optimize the parameters to adapt code to the specific noise. We consider the five-qubit code as an example and give a VGQEC code that can connect the repetition code and [[5, 1, 3]] code. Under a specific noise process, we show the optimized VGQEC code has an advantage in fidelity and is gradually adjusted from the five-qubit repetition code to the [[5, 1, 3]] code.

We also introduce a practical scheme to construct and optimize the VGQEC codes, which outputs the corresponding encoding and recovery maps without prior information on the noise model. We numerically simulate the performance of the scheme under amplitude damping
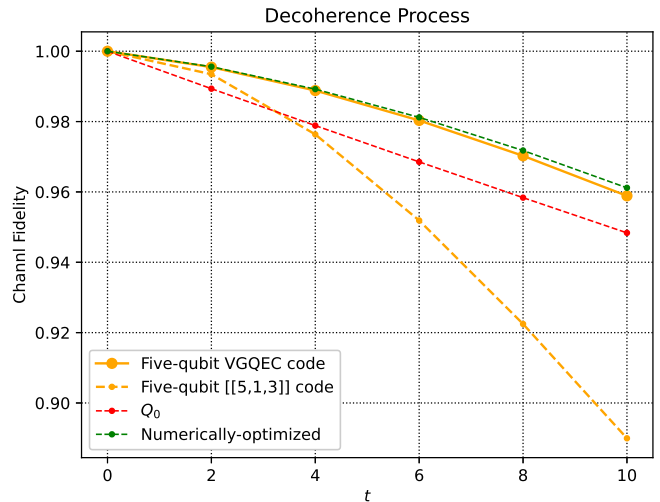

Figure 5. The performances of optimized VGQEC codes and original codes under asymmetric noise setting. The noise is set to be thermal relaxation errors on each qubit with different intensities. The intensities are selected to match the coherence time of the real *IBM-LIMA* machine, in Table I. Q_0 in the figure represents the channel fidelity of unprotected channel over the best quality single qubit Q_0. The numerically-optimized results are obtained using the iterated convex optimization [35].

noise and thermal relaxation process. In both cases, the optimized VGQEC codes show a significant improvement compared to the original codes.

Our work thus opens an avenue for designing device-tailored codes. However, many problems need further theoretical analysis and are still open. Firstly, modifying graphs, or rather, the placement of embedded parameters, has considerable freedom. Apart from some simple heuristics, we lack theoretical analysis to guide how to embed the parameters in graphs optimally. Secondly, the recovery map of VGQEC is difficult to obtain, especially in the case of non-stabilizer code. There are some options such as the optimal recovery maps derived through SDP and Petz recovery map, as well as the variational quantum circuits to implement the recovery map. Nevertheless, these recovery maps necessitate either noise modeling or incur significant training costs. Further investigation into the recovery map of VGQEC is therefore warranted. Thirdly, several important properties of VGQEC, such as the implementation of logical operators, the error threshold, and the circuit complexity of encoding, are still unknown.

ACKNOWLEDGEMENT

[1] M. A. Nielsen and I. Chuang, "Quantum computation and quantum information," 2002.

[2] P. W. Shor, "Polynomial-time algorithms for prime factorization and discrete logarithms on a quantum computer," *SIAM review*, vol. 41, no. 2, pp. 303–332, 1999.

[3] L. K. Grover, "A fast quantum mechanical algorithm for database search," in *Proceedings of the twenty-eighth annual ACM symposium on Theory of computing*, pp. 212–219, 1996.

[4] V. Dunjko, Y. Ge, and J. I. Cirac, "Computational speedups using small quantum devices," *Physical review letters*, vol. 121, no. 25, p. 250501, 2018.

[5] E. Campbell, A. Khurana, and A. Montanaro, "Applying quantum algorithms to constraint satisfaction problems," *Quantum*, vol. 3, p. 167, 2019.

[6] N. C. Jones, J. D. Whitfield, P. L. McMahon, M.-H. Yung, R. Van Meter, A. Aspuru-Guzik, and Y. Yamamoto, "Faster quantum chemistry simulation on fault-tolerant quantum computers," *New Journal of Physics*, vol. 14, no. 11, p. 115023, 2012.

[7] A. W. Harrow, A. Hassidim, and S. Lloyd, "Quantum algorithm for linear systems of equations," *Physical review letters*, vol. 103, no. 15, p. 150502, 2009.

[8] B. M. Terhal, "Quantum error correction for quantum memories," *Reviews of Modern Physics*, vol. 87, no. 2, pp. 307–346, 2015.

[9] P. W. Shor, "Scheme for reducing decoherence in quantum computer memory," *Physical review A*, vol. 52, no. 4, p. R2493, 1995.

[10] D. A. Lidar and T. A. Brun, *Quantum error correction*. Cambridge university press, 2013.

[11] S. M. Girvin, "Introduction to quantum error correction and fault tolerance," *arXiv preprint arXiv:2111.08894*, 2021.

[12] A. Y. Kitaev, "Quantum computations: algorithms and error correction," *Russian Mathematical Surveys*, vol. 52, no. 6, p. 1191, 1997.

[13] A. G. Fowler, M. Mariantoni, J. M. Martinis, and A. N. Cleland, "Surface codes: Towards practical large-scale quantum computation," *Physical Review A*, vol. 86, no. 3, p. 032324, 2012.

[14] E. Dennis, A. Kitaev, A. Landahl, and J. Preskill, "Topological quantum memory," *Journal of Mathematical Physics*, vol. 43, no. 9, pp. 4452–4505, 2002.

[15] A. G. Fowler, A. M. Stephens, and P. Groszkowski, "High-threshold universal quantum computation on the surface code," *Physical Review A*, vol. 80, no. 5, p. 052312, 2009.

[16] S. B. Bravyi and A. Y. Kitaev, "Quantum codes on a lattice with boundary," *arXiv preprint quant-ph/9811052*, 1998.

[17] A. R. Calderbank and P. W. Shor, "Good quantum error-correcting codes exist," *Physical Review A*, vol. 54, no. 2, p. 1098, 1996.

[18] A. Steane, "Multiple-particle interference and quantum error correction," *Proceedings of the Royal Society of London. Series A: Mathematical, Physical and Engineering Sciences*, vol. 452, no. 1954, pp. 2551–2577, 1996.

[19] D. Gottesman, *Stabilizer codes and quantum error correction.* California Institute of Technology, 1997.

[20] A. Cross, G. Smith, J. A. Smolin, and B. Zeng, "Codeword stabilized quantum codes," in *2008 IEEE International Symposium on Information Theory*, pp. 364–368, IEEE, 2008.

[21] I. Chuang, A. Cross, G. Smith, J. Smolin, and B. Zeng, "Codeword stabilized quantum codes: Algorithm and structure," *Journal of Mathematical Physics*, vol. 50, no. 4, p. 042109, 2009.

[22] N. P. Breuckmann and J. N. Eberhardt, "Quantum low-density parity-check codes," *PRX Quantum*, vol. 2, no. 4, p. 040101, 2021.

[23] P. Panteleev and G. Kalachev, "Asymptotically good quantum and locally testable classical ldpc codes," in *Proceedings of the 54th Annual ACM SIGACT Symposium on Theory of Computing*, pp. 375–388, 2022.

[24] C. M. Dawson, H. L. Haselgrove, and M. A. Nielsen, "Noise thresholds for optical quantum computers," *Physical review letters*, vol. 96, no. 2, p. 020501, 2006.

[25] C. D. Wilen, S. Abdullah, N. Kurinsky, C. Stanford, L. Cardani, G. d'Imperio, C. Tomei, L. Faoro, L. Ioffe, C. Liu, *et al.*, "Correlated charge noise and relaxation errors in superconducting qubits," *Nature*, vol. 594, no. 7863, pp. 369–373, 2021.

[26] Q. Guo, Y.-Y. Zhao, M. Grassl, X. Nie, G.-Y. Xiang, T. Xin, Z.-Q. Yin, and B. Zeng, "Testing a quantum error-correcting code on various platforms," *Science Bulletin*, vol. 66, no. 1, pp. 29–35, 2021.

[27] D. W. Leung, M. A. Nielsen, I. L. Chuang, and Y. Yamamoto, "Approximate quantum error correction can lead to better codes," *Physical Review A*, vol. 56, no. 4, p. 2567, 1997.

[28] P. T. Cochrane, G. J. Milburn, and W. J. Munro, "Macroscopically distinct quantum-superposition states as a bosonic code for amplitude damping," *Physical Review A*, vol. 59, no. 4, p. 2631, 1999.

[29] L. Li, C.-L. Zou, V. V. Albert, S. Muralidharan, S. Girvin, and L. Jiang, "Cat codes with optimal decoherence suppression for a lossy bosonic channel," *Physical review letters*, vol. 119, no. 3, p. 030502, 2017.

[30] M. H. Michael, M. Silveri, R. Brierley, V. V. Albert, J. Salmilehto, L. Jiang, and S. M. Girvin, "New class of quantum error-correcting codes for a bosonic mode," *Physical Review X*, vol. 6, no. 3, p. 031006, 2016.

[31] A. S. Fletcher, P. W. Shor, and M. Z. Win, "Channel-adapted quantum error correction for the amplitude damping channel," *IEEE Transactions on Information Theory*, vol. 54, no. 12, pp. 5705–5718, 2008.

[32] R. L. Kosut, A. Shabani, and D. A. Lidar, "Robust quantum error correction via convex optimization," *Physical review letters*, vol. 100, no. 2, p. 020502, 2008.

[33] S. Taghavi, R. L. Kosut, and D. A. Lidar, "Channel-optimized quantum error correction," *IEEE transactions*

on information theory, vol. 56, no. 3, pp. 1461–1473, 2010.

[34] M. Berta, F. Borderi, O. Fawzi, and V. B. Scholz, "Semidefinite programming hierarchies for constrained bilinear optimization," *Mathematical Programming*, pp. 1–49, 2022.

[35] R. L. Kosut and D. A. Lidar, "Quantum error correction via convex optimization," *Quantum Information Processing*, vol. 8, no. 5, pp. 443–459, 2009.

[36] A. S. Fletcher, P. W. Shor, and M. Z. Win, "Structured near-optimal channel-adapted quantum error correction," *Physical Review A*, vol. 77, no. 1, p. 012320, 2008.

[37] M. Reimpell and R. F. Werner, "Iterative optimization of quantum error correcting codes," *Physical review letters*, vol. 94, no. 8, p. 080501, 2005.

[38] H. P. Nautrup, N. Delfosse, V. Dunjko, H. J. Briegel, and N. Friis, "Optimizing quantum error correction codes with reinforcement learning," *Quantum*, vol. 3, p. 215, 2019.

[39] T. Fösel, P. Tighineanu, T. Weiss, and F. Marquardt, "Reinforcement learning with neural networks for quantum feedback," *Physical Review X*, vol. 8, no. 3, p. 031084, 2018.

[40] D. F. Locher, L. Cardarelli, and M. Müller, "Quantum error correction with quantum autoencoders," *Quantum*, vol. 7, p. 942, 2023.

[41] J. Bausch and F. Leditzky, "Quantum codes from neural networks," *New Journal of Physics*, vol. 22, no. 2, p. 023005, 2020.

[42] P. D. Johnson, J. Romero, J. Olson, Y. Cao, and A. Aspuru-Guzik, "Qvector: an algorithm for device-tailored quantum error correction," *arXiv preprint arXiv:1711.02249*, 2017.

[43] C. Cao, C. Zhang, Z. Wu, M. Grassl, and B. Zeng, "Quantum variational learning for quantum error-correcting codes," *arXiv preprint arXiv:2204.03560*, 2022.

[44] F. Zoratti, G. De Palma, B. Kiani, Q. T. Nguyen, M. Marvian, S. Lloyd, and V. Giovannetti, "Improving the speed of variational quantum algorithms for quantum error correction," *Physical Review A*, vol. 108, no. 2, p. 022611, 2023.

[45] A. M. Jaffe and Z. Liu, "Mathematical picture language program," *Proceedings of the National Academy of Sciences*, vol. 115, no. 1, pp. 81–86, 2018.

[46] Z. Liu, A. Wozniakowski, and A. M. Jaffe, "Quon 3d language for quantum information," *Proceedings of the National Academy of Sciences*, vol. 114, no. 10, pp. 2497–2502, 2017.

[47] Z. Liu, "Quantized graphs and quantum error correction," *arXiv preprint arXiv:1910.12065*, 2019.

[48] G. Benenti and G. Strini, "Computing the distance between quantum channels: usefulness of the fano representation," *Journal of Physics B: Atomic, Molecular and Optical Physics*, vol. 43, no. 21, p. 215508, 2010.

[49] B. Schumacher, "Sending entanglement through noisy quantum channels," *Physical Review A*, vol. 54, no. 4, p. 2614, 1996.

[50] C. Bény and O. Oreshkov, "General conditions for approximate quantum error correction and near-optimal recovery channels," *Phys. Rev. Lett.*, vol. 104, p. 120501, Mar 2010.

[51] D. Bures, "An extension of kakutani's theorem on infinite product measures to the tensor product of semifinite w*-algebras," *Transactions of the American Mathematical Society*, vol. 135, pp. 199–212, 1969.

[52] E. Knill and R. Laflamme, "Theory of quantum error-correcting codes," *Physical Review A*, vol. 55, no. 2, p. 900, 1997.

[53] A. S. Fletcher, P. W. Shor, and M. Z. Win, "Optimum quantum error recovery using semidefinite programming," *Physical Review A*, vol. 75, no. 1, p. 012338, 2007.

[54] H. Barnum and E. Knill, "Reversing quantum dynamics with near-optimal quantum and classical fidelity," *Journal of Mathematical Physics*, vol. 43, no. 5, pp. 2097–2106, 2002.

[55] A. Gilyén, S. Lloyd, I. Marvian, Y. Quek, and M. M. Wilde, "Quantum algorithm for petz recovery channels and pretty good measurements," *Physical Review Letters*, vol. 128, no. 22, p. 220502, 2022.

[56] J. Preskill, "Quantum computing in the nisq era and beyond," *Quantum*, vol. 2, p. 79, 2018.

[57] IBM company, "Ibm quantum compute resources website." `https://quantum-computing.ibm.com/services/resources?system=ibmq_lima` Accessed October 14, 2022.

[58] J. A. Nelder and R. Mead, "A simplex method for function minimization," *The computer journal*, vol. 7, no. 4, pp. 308–313, 1965.

[59] C.-N. Yang, "Some exact results for the many-body problem in one dimension with repulsive delta-function interaction," *Physical Review Letters*, vol. 19, no. 23, p. 1312, 1967.

[60] R. J. Baxter, *Exactly solved models in statistical mechanics*. Elsevier, 2016.

[61] C. Dankert, R. Cleve, J. Emerson, and E. Livine, "Exact and approximate unitary 2-designs and their application to fidelity estimation," *Physical Review A*, vol. 80, no. 1, p. 012304, 2009.

[62] Y. Nakata, C. Hirche, C. Morgan, and A. Winter, "Unitary 2-designs from random x-and z-diagonal unitaries," *Journal of Mathematical Physics*, vol. 58, no. 5, p. 052203, 2017.

[63] A. W. Harrow and S. Mehraban, "Approximate unitary t-designs by short random quantum circuits using nearest-neighbor and long-range gates," *Communications in Mathematical Physics*, vol. 401, no. 2, pp. 1531–1626, 2023.

[64] J. C. Spall, "Implementation of the simultaneous perturbation algorithm for stochastic optimization," *IEEE Transactions on aerospace and electronic systems*, vol. 34, no. 3, pp. 817–823, 1998.

[65] D. P. Kingma and J. Ba, "Adam: A method for stochastic optimization," *arXiv preprint arXiv:1412.6980*, 2014.

[66] D. C. Liu and J. Nocedal, "On the limited memory bfgs method for large scale optimization," *Mathematical programming*, vol. 45, no. 1, pp. 503–528, 1989.

CONTENTS

Appendix A: Quon language

The quon language [45–47] provides a mathematical picture language to study quantum information. The pictures are given by braided charged strings in three-dimensional space. In the following, we introduce the basic computational rules of Quon language and show how to represent quantum error correction codes in Quon language.
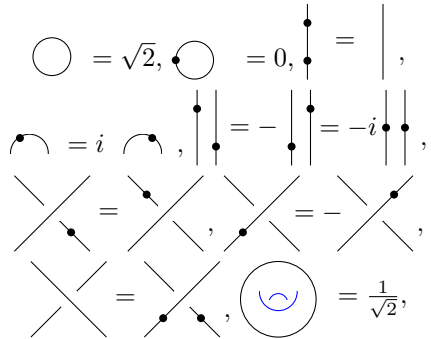
In Quon, the 1-qubit XYZ computational bases are represented by the following diagrams in a hemisphere:

$$
\sqrt{2}\,|0\rangle_Z = \sqrt{2}\,|0\rangle = \quad \frown \quad \frown \,,
$$
$$
\sqrt{2}\,|0\rangle_Y = |0\rangle + i\,|1\rangle = \overbrace{\quad\frown\quad} \,,
$$
$$
\sqrt{2}\,|0\rangle_X = |0\rangle + |1\rangle = \overbrace{\quad \frown \quad}\,.
$$
(A1)

Correspondingly, $|1\rangle_Z$, $|1\rangle_Y$, $|1\rangle_X$ are obtained by adding a pair of charges separately to the two strings in $|0\rangle_Z$, $|0\rangle_Y$, $|0\rangle_X$, respectively. Pauli X, Y, and Z gates are represented by the following diagrams in a cylinder:

$$
\begin{aligned}
I &= \Big|\;\Big|\;\Big|\;\Big| = \dot{\Big|}\;\dot{\Big|}\;\dot{\Big|}\;\dot{\Big|}\,, \\
Z &= \dot{\Big|}\;\dot{\Big|}\;\Big|\;\Big| = \Big|\;\Big|\;\dot{\Big|}\;\dot{\Big|}\,, \\
Y &= \dot{\Big|}\;\Big|\;\dot{\Big|}\;\Big| = \Big|\;\dot{\Big|}\;\Big|\;\dot{\Big|}\,, \\
X &= \dot{\Big|}\;\Big|\;\Big|\;\dot{\Big|} = \Big|\;\dot{\Big|}\;\dot{\Big|}\;\Big|\,.
\end{aligned}
$$
(A2)

In addition, there are some relevant properties of the quon language:

$$
\text{(A3)}
$$

where the blue graphic in the last diagram represents a hole.

The pictures in the bulk represent gates projectively and the pictures on the boundary represent states linearly. For example, the equality $\langle 0| X |0\rangle = 0$ can be represented by the following diagram:
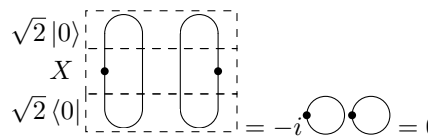
$$
\sqrt{2}\,|0\rangle \quad X \quad \sqrt{2}\,\langle 0| \quad = -i \bigcirc \bullet \bigcirc = 0 \tag{A4}
$$

Appendix B: Quon graph for Quantum Error Correction Codes

In [47], the author introduces a systematic method for representing stabilizer codes using graphs. This method facilitates the analysis of specific noise effects through graphical representation, thereby enabling a topological understanding of error correction capabilities.

We take the $[[5,1,3]]$ code as an example. It encodes one logical qubit into five physical qubits, and corrects one-qubit arbitrary error. The $[[5,1,3]]$ code is a stabilizer code [19] and the code can be fully described by its stabilizer group. The stabilizer group of the $[[5,1,3]]$ code has the generators:

$$
\{X_2 Z_3 Z_4 X_5, X_1 X_3 Z_4 Z_5, Z_1 X_2 X_4 Z_5, Z_1 Z_2 X_3 X_5\}. \tag{B1}
$$

The generators of the stabilizer group (B1) are corresponded to the four cycles with even-length:

$$
\begin{aligned}
L_1 &: 2 \longrightarrow 4 \longrightarrow 3 \longrightarrow 5 \longrightarrow 2,\\
L_2 &: 3 \longrightarrow 5 \longrightarrow 4 \longrightarrow 1 \longrightarrow 3,\\
L_3 &: 4 \longrightarrow 1 \longrightarrow 5 \longrightarrow 2 \longrightarrow 4,\\
L_5 &: 5 \longrightarrow 2 \longrightarrow 1 \longrightarrow 3 \longrightarrow 5.
\end{aligned}
$$

Specifically, considering the cycle $L_1 : 2 \longrightarrow 4 \longrightarrow 3 \longrightarrow 5 \longrightarrow 2$, we define the *cycle operator* O_{L_1} acting on the Quon graph, and adding pairs of charges on the cycle L_1. By diagrammatic operator using Eq. (A2), we have $O_{L_1} = X_2 Z_3 Z_4 X_5$. The cycle operator O_{L_1} stabilizes the encoded quantum state $|0\rangle_L, |1\rangle_L$, because each edge in the cycle L_1 contains two changes, which will cancel each other as illustrated in Fig. 6. It is worth noting that the requirement for cycle length even-length cannot be ignored here. In actuality, for any stabilizer code, a stabilizer corresponds to a cycle in the Quon graph of its encoding map that does not enclose the logical qubit. For simplicity, we did not present the Quon graph of the encoding map for the $[[5,1,3]]$ code here. The even-length constraint is equivalent to the cycle that does not enclose the logical qubit for the $[[5,1,3]]$ code.

The idea of VGQEC is to introduce parameters to the Quon graph. The definition of parameters in Quon graph is shown in Fig. 7. Parallel strings can be treated as a crossing of the strings with parameter $\alpha = 0$, and every crossing of the strings in the Quon graph contains an implicit parameter $-\frac{\pi}{2}$ or $\frac{\pi}{2}$ corresponding to a positive or negative crossing, respectively. One potential modification is to replace the implicit parameters of the crossings with explicit variables, thereby enabling variability in braid crossings. In addition to deforming already existing crossings, we can add variable crossing to graphs, by replacing parallel strings with variable crossings. These operations make it possible to continuously change the construction of the Quon graph, such as changing the connection between discs, modifying the position of crossings, adding or deleting variable crossings, etc.
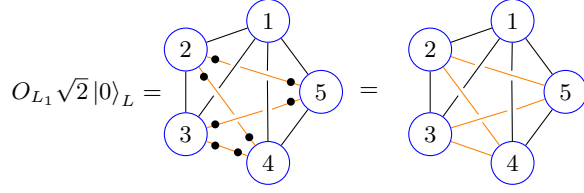
Figure 6. Cycle Operator as Stabilizers: The cycle operator O_{L_1} corresponding to the cycle L_1 stabilizes the encoded quantum state. Here, the marks of starting position are ignored.

Figure 7. Graphical interpretation of braids crossings: (a) Variable braids crossing with parameter α. When the crossing parameter $\alpha = 0$, the crossed strings will be transformed into parallel strings. As shown in (b) and (c), the positive and negative braids crossings differ from variable braids crossings with parameters $-\frac{\pi}{2}$ and $\frac{\pi}{2}$ by a global phase $\omega^{-\frac{1}{2}} = (\frac{1+i}{\sqrt{2}})^{-\frac{1}{2}}$ that can be ignored, respectively.

In Sec. III, we construct a VGQEC from the Quon graph Fig. 1(b) with parameters $\{\alpha_i\}_{i=1,\ldots,5}$. We claim that the encoding circuit of the VGQEC code is Fig. 9. This is because R_X and R_{ZZ} have graphical representations presented in Fig. 8. Notice that if the inverse of $U_{\mathcal{E}}$ in Fig. 9 is applied to the logical state $|0\rangle_L$ of the VGQEC code, it would result in state $|+\rangle^{\otimes 5}$, shown in Fig. 10. Similarly, the result of the inverse of $U_{\mathcal{E}}$ applying to the logical state $|1\rangle_L$ of the VGQEC code is $|-\rangle^{\otimes 5}$. And the encoding map of $|\pm\rangle^{\otimes 5}$ is exactly $\mathcal{E}_c$ in Fig. 9. Thus we have verified that the encoding circuit of the VGQEC code is Fig. 9.

Figure 8. Quon diagram representation of Pauli rotation gates R_X and R_{ZZ}. This can be verified by applying the diagrammatic operator to the computational basis Eq. (A1).

Appendix C: Details of interpolation from five-qubit repetition code to the $[[5,1,3]]$ code

In Sec. III we modify the five-qubit $[[5,1,3]]$ code, getting a VGQEC code with parameters $\{\alpha_i\}_{i=1,\ldots,5}$. By transforming the Quon graph into a quantum circuit, we get the encoding circuit of the VGQEC code (shown in Fig. 9), denoted as $\mathcal{E}'$. We simulate the performance of the VGQEC code over a specific noise evolution process.

In this simulation, the noise is a composite channel of three parts $\mathcal{N} = \mathcal{N}_3 \circ \mathcal{N}_2 \circ \mathcal{N}_1^{\eta}$, a variable part $\mathcal{N}_1^{\eta}$ and two fixed parts $\mathcal{N}_2, \mathcal{N}_3$. The variable noise channel $\mathcal{N}_1^{\eta}$ is defined as a tensor $\mathcal{N}_s^{\eta \otimes 5}$ of a single-qubit noise channel:

$$\mathcal{N}_s^{\eta}(\rho) = 0.05(Z\rho Z + \eta X\rho X + \eta Y\rho Y) + (0.95 - 0.1\eta)\rho. \tag{C1}$$

This is a linear interpolation from the dephasing channel to the depolarization channel. The fixed noise channel $\mathcal{N}_2$ is modeled as a two-qubit correlated Pauli-X error model. Specifically, we apply quantum channel:

$$\mathcal{N}_{2,i}(\rho) = (1 - p_{xx})\rho + p_{xx}X_i X_{i+1}\rho X_i X_{i+1} \tag{C2}$$

for pairs of nearby qubits, where $i \in \{1,2,3,4\}$ and $p_{xx} = 0.05$. And the fixed channel $\mathcal{N}_3 = \mathcal{N}_s^{ad \otimes 5}$ is a tensor of
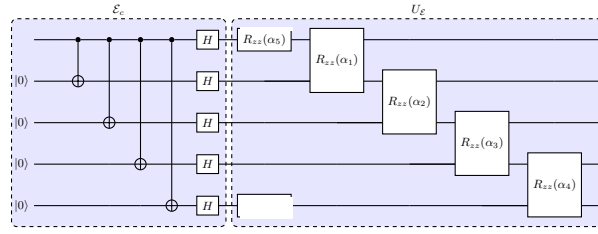
Figure 9. The encoding circuit for an optional five-qubit VGQEC code: The encoding map can be divided into fixed map $\mathcal{E}_c$ and variational quantum circuit $U_\mathcal{E}$. The Quon graph of the VGQEC code is shown in Fig. 1(b).
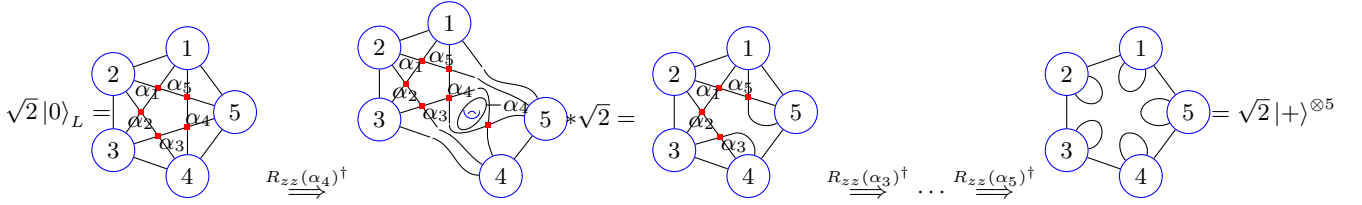

Figure 10. The state $|+\rangle^{\otimes 5}$ is prepared by applying the inverse of the unitary operation $U_\mathcal{E}$, as depicted in circuit Fig. 9, to the logical state $|0\rangle_L$. In this figure, the global phases are omitted. The first arrow represents the applying of $R_{zz}(\alpha_4)^\dagger$ to the logical state $|0\rangle_L$, which is to gluing the graph of R_{zz} as shown in Fig. 8 to physical qubits 4 and 5. The gluing operation creates a hole (shown in blue graphic), which contain in a circle. The subgraph of hole in circle is equivalent to $\frac{1}{\sqrt{2}}$, by the property in Eq. (A3). And the factor $\sqrt{2}$ comes from the graph of R_{zz} gate, as shown in Fig. 8. The first equation is given by replacing the hole with the factor $\frac{1}{\sqrt{2}}$, as well as canceling the two crossings with parameters α_4 and $-\alpha_4$.

single-qubit amplitude damping channel:

$$\mathcal{N}_s^{ad}(\rho) = \sum_{k=0,1} E_k \rho E_k^\dagger,$$

$$E_0 = \begin{bmatrix} 1 & 0 \\ 0 & \sqrt{1-\gamma} \end{bmatrix} \quad E_1 = \begin{bmatrix} 0 & \sqrt{\gamma} \\ 0 & 0 \end{bmatrix},$$

where γ is set as 0.05.

When the value of crossing parameters $\{\alpha_i\}_{i=1,\dots,5}$ are given, there exists an optimal recovery map $\mathcal{R}_{opt}$ in (5) to maximize the channel fidelity $F_C(\mathcal{R} \circ \mathcal{N} \circ \mathcal{E}')$. We take the channel fidelity of $\mathcal{R}_{opt} \circ \mathcal{N} \circ \mathcal{E}'$ as the object function and input it to *Nelder-Mead* algorithm [58]. The classical optimizer optimizes the parameters $\{\alpha_i\}_{i=1,\dots,5}$ and improves the channel fidelity, finally obtaining the trained VGQEC code. In our numerical results, for any η, the parameters are initialized by random numbers, we repeat the random initialization and training process 20 times and select the result with the highest fidelity. For a fair comparison, we also use the optimal recovery map obtained by SDP to decode the five-qubit repetition code and $[[5, 1, 3]]$ code, and calculate the channel fidelity of the two codes.

Appendix D: Construct VGQEC scheme using variational quantum circuits

As demonstrated in Sec. III, a stabilizer code can be represented by Quon graph, thereby constructing a VGQEC code by introducing parameters to the graph. Typically, the encoding map $\mathcal{E}'$ of a VGQEC code is derived directly from the Quon graph. However, transforming a complex Quon graph into a quantum circuit is not always an easy task.

Alternatively, for a given code, besides pre-embedding parameters on the Quon diagram of the code to get VGQEC, we can also append a variational quantum circuit $U_\mathcal{E}$ directly after the encoding mapping of the code $\mathcal{E}_c$ to establish the encoding scheme $\mathcal{E}' = U_\mathcal{E} \circ \mathcal{E}_c$. The variational quantum circuit $U_\mathcal{E}$ followed by $\mathcal{E}_c$ can viewed as a variable graphical structure glued to physical qubit discs in the Quon graph, resulting in a VGQEC code.

On the other side, we hope to construct a variational quantum circuit as the recovery map of the VGQEC code, which holds the ability to implement the original recovery map of the given code. The recovery map $\mathcal{R}'$ of the VGQEC code is constructed by appending $2k$ auxiliary qubits and applying a variational quantum circuit $U_\mathcal{R}$ to the system,
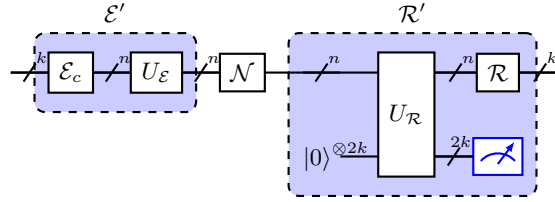
Figure 11. The encoding map $\mathcal{E}' : \mathcal{H}^{\otimes k} \to \mathcal{H}^{\otimes n}$ is the composition of the original encoding map $\mathcal{E}_c$ and a variational quantum circuit $U_{\mathcal{E}}$. The recovery map $\mathcal{R}' : \mathcal{H}^{\otimes n} \to \mathcal{H}^{\otimes k}$ is made by introducing $2k$ auxiliary qubits, then acting a variational quantum circuit $U_{\mathcal{R}}$, after which the auxiliary qubits are traced out and finally the original recovery map $\mathcal{R}$ is acted.
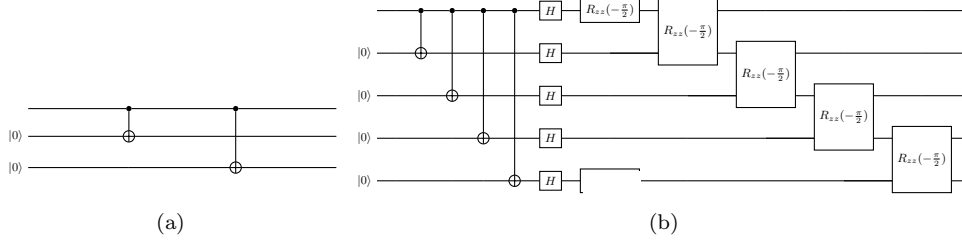

Figure 12. The fixed part $\mathcal{E}_c$ in encoding map of the VGQEC codes: (a) For the three-qubit VGQEC code modified from repetition codes, the fixed part is the original encoding maps. The figure shows the circuit for the three-qubit case. (b) For the five-qubit VGQEC code, it is modified from $[[5,1,3]]$ codes, the fixed part is the encoding map of the $[[5,1,3]]$ code.

followed by a measurement of the auxiliary qubits and the original recovery map $\mathcal{R}$. The whole error correction scheme is shown in Fig. 11.

We investigate the performance of three-qubit and five-qubit VGQEC codes modified from the three-qubit repetition code and the five-qubit $[[5,1,3]]$ code, respectively. The VGQEC codes in the simulations are constructed by gluing a specially designed structure to the physical qubit discs in the Quon graphs. At this point, the encoding maps $\mathcal{E}'$ have a decomposition $\mathcal{E}' = U_{\mathcal{E}} \circ \mathcal{E}_c$, where $\mathcal{E}_c$ are the fixed encoding maps of the original codes as show in Fig. 12 and $U_{\mathcal{E}}$ are variational quantum circuits.

In the above two VGQEC codes, the structure of variational quantum circuits $U_{\mathcal{E}}$ in the encoding map is inspired by a specially designed Quon graph M_u. For the case of n qubits, M_u has $4n$ strings and $n(2n-1)$ braids crossings with parameters. Specifically, the graph features $2n$ external strings surrounding it, while the remaining $2n$ internal strings intertwine within the graph itself. If we use $i \to j$ to indicate that the $i-th$ internal string at the top will reach the $j-th$ position at the bottom in the graph. Then the linkage relationship of the strings in the graph are $1 \to 2n$, $2 \to 2n-1$, ..., $n \to n+1$. There is an example for $n = 3$, shown in Fig. 13.
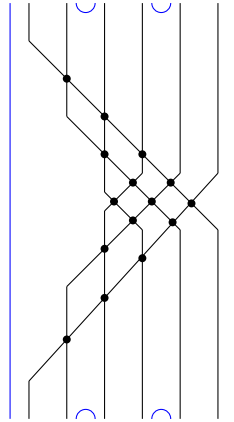

Figure 13. "Universal" graph M_u for $n = 3$: every point in the figure represents a braid crossing with variable. The black and blue strings in the figure represent internal and external strings, respectively, with internal strings intersecting pairwise.

The reason for considering M_u is that, the internal $2n$ strings intersect pairwise, offering great structural flexibility

when adjusting parameters. In fact, this diagram gives a "universal" graph for the internal $2n$ strings. This means that for any geometry structure of the internal strings, we can use the M_u to represent it by setting property parameters. Firstly, any geometry structure of the internal strings can be decomposed into a series of braid crossings on adjacent strings. Then the universal property of M_u can be illustrated by using *Yang-Baxter* equation [59, 60] (Fig. 14) to absorb any braid crossings into M_u. Suppose there is a braid crossing on the 2-nd and 3-rd positions, then we can use the Yang-Baxter equation to absorb them into M_u, as shown in Fig. 15. The other advantage of M_u is that it can be easily constructed by a variational quantum circuit, which is composed of a series of R_{ZZ} and R_X gates. This makes it easy to implement in the real quantum device.
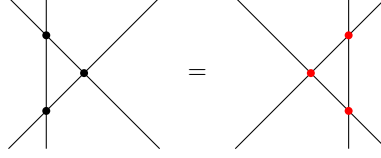

Figure 14. Graphical interpretation of the Yang-Baxter equation: The black dots in the figure indicate the braid crossings with parameters. We can move the vertical string across the middle crossing to the right side. Simultaneously change the three crossing parameters, with red dots indicating the new parameters.
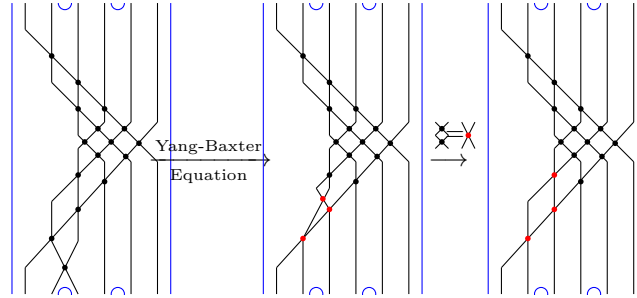

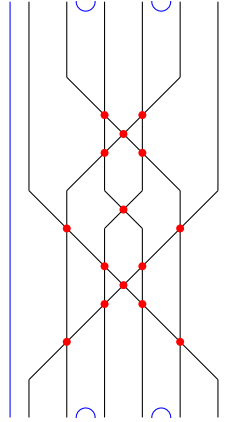Figure 15. The graph represents the process of absorbing $R_{Z_1 Z_2}$ into M_u.

Figure 16. Left-right symmetric form of M_u for $n = 3$: reshaped from Fig. 13 by using the Yang-Baxter equation Fig. 14.

The graph M_u with parameters constructs a "universal" set. However, this circuit is not symmetric and the asymmetry of the variational quantum circuit may cause some difficulties in the process of optimizing the parameters. To overcome this problem, we use the Yang-Baxter equation to reshape this graph into a left-right symmetric form, as shown in Fig. 16. Using the relation in Fig. 8, we can transform the left-right symmetric form of M_u into a variational quantum circuit consisting of R_{ZZ} and R_X gates.

The variational quantum circuit $U_{\mathcal{E}}$ in encoding map $\mathcal{E}_c$ is chosen to be a composition of a layer of R_z rotations to each qubit, a circuit block transformed from the symmetrized M_u (Fig. 16) and another layer of R_z rotations at the last. For $n = 5$, the variational quantum circuit $U_{\mathcal{E}}$ is shown in Fig. 17(a).

(a)variational quantum circuit $U_\mathcal{E}$ (b)variational quantum circuit $U_\mathcal{R}$
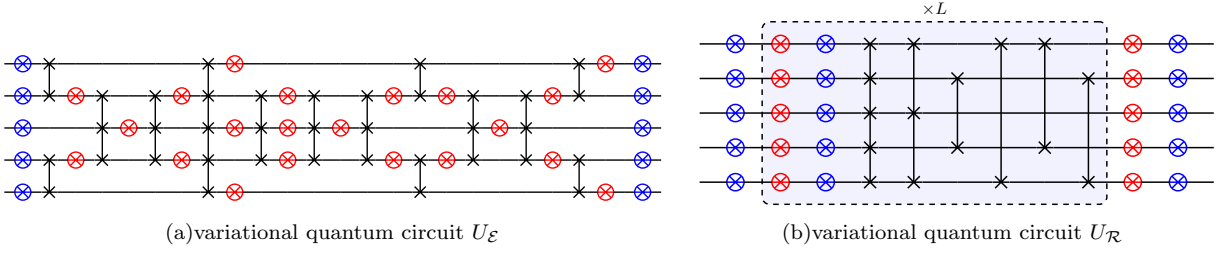
Figure 17. (a) The variational quantum circuit $U_\mathcal{E}$ contains of a layer of R_z rotations to each qubit, a circuit block from the symmetrized M_u (Fig. 16) and another layer of R_z rotations at the last. (b) The variational quantum circuit $U_\mathcal{R}$: We apply R_X-R_Z rotations to each qubit, R_{ZZ} gates to all pairs of qubits and repeat the previous operation L times. Finally apply R_Z rotations and R_X-R_Z rotations to each qubit at at the beginning and end of the circuit, respectively. For convenience, the double qubit gate drawn in black represents R_{ZZ}, the single-qubit gate drawn in red circle is R_X and the single qubit gate drawn in blue circle is R_Z.

In our simulations, we tested the VGQEC codes with single logical qubit. When the variational quantum circuit at the encoding map $U_\mathcal{E}$ has n qubits, the variational quantum circuit in the recovery map $U_\mathcal{R}$ has $n+2$ qubits. The structure of variational quantum circuit $U_\mathcal{R}$ we applied in the simulation is shown in Fig. 17(b). The variational quantum circuit $U_\mathcal{R}$ can be decomposed into a layer of R_z rotations, L repetitive circuit blocks and alternating layers of single-qubit rotations R_X-R_Z acting on all qubits. Every circuit block contains an alternating R_x-R_z rotations layer and interactions R_{ZZ} acting on all pairs of qubits. In principle, any n-qubit unitary evolution can be realized by this ansatz with a sufficiently large L since $\{R_X, R_Z, R_{ZZ}\}$ is a universal quantum gate set. In our numerical results, the number of Repeatitation in $U_\mathcal{R}$ is chosen to be $L=3$.

To tailor the VGQEC code for a particular noise channel, the *average entanglement fidelity* (1) is employed as the metric for assessing the efficacy of error correction schemes pertinent to that channel. The quantum channel $\mathcal{M}$ in (1) is chosen to be the noise channel with VGQEC code protection $\mathcal{M} = \mathcal{R}' \circ \mathcal{N} \circ \mathcal{E}'$, where $\mathcal{E}'$ and $\mathcal{R}'$ are the encoding and recovery map of the VGQEC code. Here, the variable operators $U_\mathcal{E}$, $U_\mathcal{R}$ in $\mathcal{E}'$ and $\mathcal{R}'$ are implemented by variational quantum circuits with parameters vectors α, β, respectively.

In the optimization process, the objective function for optimization is defined as the average entanglement fidelity of protected channel $\mathcal{M}$ and pure state ensemble $E = \{|\psi\rangle \langle\psi|, \mu_H(|\psi\rangle)\}$ with *Haar measure* μ_H. Specifically, the objective function is constructed as:

$$F(\alpha, \beta) = \mathbb{E}_{|\psi\rangle \sim \mu_H} F_e(|\psi\rangle \langle\psi|, \mathcal{M}). \tag{D1}$$

Now, we illustrate a subroutine to estimate the average entanglement fidelity (D1). The fidelity estimation algorithm first appeared in [42]. An important step in average entanglement fidelity estimation is to generate random quantum states $|\psi\rangle$. This can be done by acting operator U on the initial quantum state, where U is sampled randomly from the Haar distribution. However, since the fidelity depends only on the second-order moments of the distribution, there is no need to sample U from the Haar distribution, but from an efficiently implementable unitary 2-design distribution [61]. A unitary 2-design is a set X on the unitary group $\mathcal{U}(d)$ satisfying

$$\frac{1}{|X|} \sum_{U \in X} U^{\otimes 2} \otimes (U^\dagger)^{\otimes 2} = \int_{\mathcal{U}(d)} U^{\otimes 2} \otimes (U^\dagger)^{\otimes 2} d\mu_H(U). \tag{D2}$$

With a 2-design X, the average entanglement fidelity (D1) of the channel $\mathcal{M}$ is written as

$$F(\alpha, \beta) = \frac{1}{|X|} \sum_{U \in X} \langle 0| U^\dagger \mathcal{M}(U |0\rangle \langle 0| U^\dagger) U |0\rangle. \tag{D3}$$

The average entanglement fidelity can be estimated by sampling 2-design circuits U, getting random states $|\psi\rangle$ by applying U to $|0\rangle^{\otimes k}$, then performing the quantum channel $\mathcal{M}$ on $|\psi\rangle$, applying the inverse of U and measuring all qubits in the computational basis. The probability of measuring all-0 outcomes is the average entanglement fidelity. The all-0 outcome and the non-all-0 outcome can be considered as a binary sample, so the estimated probabilities have standard deviation $\mathcal{O}(\frac{1}{\sqrt{N}})$ where N is the number of samples. The schematic of the algorithm is shown in Fig. 18.

In some cases, it may prove advantageous to utilize an approximate unitary 2-design. A noteworthy example is the ϵ-approximate 2-design [62, 63], and is notably straightforward to execute.
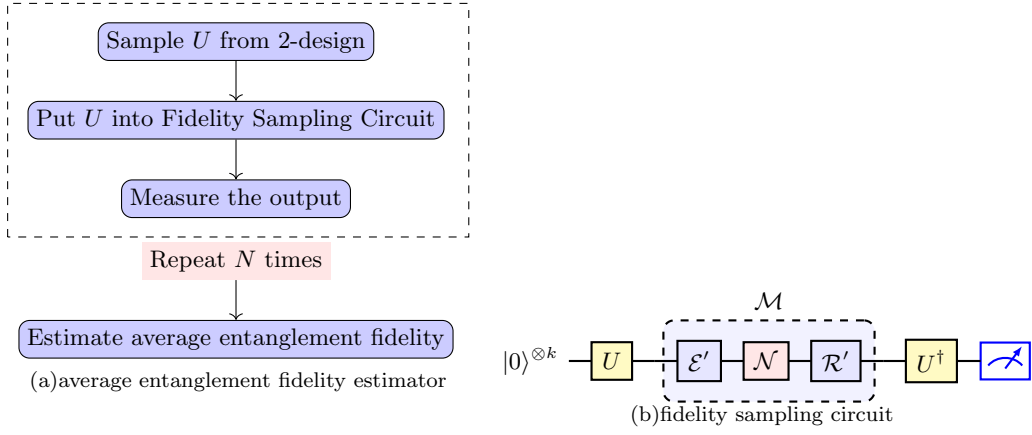
Figure 18. Schematic illustration of Fidelity Estimation: (a) average entanglement fidelity Estimator: The average entanglement fidelity estimator samples a unitary U from the 2-design and then puts U into the fidelity sampling circuit to get the outcomes of the circuit. Repeat this process N times, estimated average entanglement fidelity is the probability of all-0 output. (b) Fidelity Sampling Circuit: Random quantum states are constructed by U acting on $|0\rangle$, after the random state passes through $\mathcal{M}$ and $U^{\dagger}$, and then measured on the computational basis.

After estimating the average entanglement fidelity, we take the objective function as the input into the classical optimization algorithm such as *SPSA* [64], *ADAM* [65] or *L-BFGS* [66] to maximize the average entanglement fidelity. After optimization, the classical optimizer outputs the optimized parameters α_{opt}, β_{opt}. The encoding and recovery maps of the optimized VGQEC code are

$$\mathcal{E}_{out} = U_{\mathcal{E}}(\alpha_{opt}) \circ \mathcal{E}_c, \tag{D4}$$
$$\mathcal{R}_{out} = \mathcal{R} \circ U_{\mathcal{R}}(\beta_{opt}). \tag{D5}$$

The optimized value $F(\alpha_{opt}, \beta_{opt})$ is the average entanglement fidelity of the noise channel with the VGQEC code protection.

Appendix E: Details of numerical results

In Sec. IV, we simulated our scheme by modifying several few-qubit codes to adapt to specific noise models. In the simulations, the average entanglement fidelity in object function was computed over the projective 2-design quantum states set $\left\{ |0\rangle, \frac{1}{\sqrt{3}}|0\rangle + \sqrt{\frac{2}{3}}|1\rangle, \frac{1}{\sqrt{3}}|0\rangle + \sqrt{\frac{2}{3}}e^{\frac{i2\pi}{3}}|1\rangle, \frac{1}{\sqrt{3}}|0\rangle + \sqrt{\frac{2}{3}}e^{\frac{i4\pi}{3}}|1\rangle \right\}$. For classical optimizer, we employed *L-BFGS* [66] to optimize parameters.

Similar to the previous numerical results, our numerical explorations in scheme simulations indicated that the object function might contain several local maximum points. Adopting the same strategy as before, for each noise intensity, the parameters are initialized by generating 50 sets of random numbers and we select the result with the highest fidelity after the optimization process.

For comparison purposes, we plot the numerically-optimized results obtained by the iterated convex optimization method [35] for the asymmetrical thermal relaxation process. The main idea is that for a given noise channel, finding the optimal recovery map to maximum channel fidelity when fixing the encoding map is a semi-definite program (SDP). Similarly, finding the best encoding map when fixing the recovery map is also an SDP. In practice, we first randomly choose an initial encoding map and then solve the SDP to find the optimal recovery map. Then, setting the recovery map to this optimized one, solving the SDP again to find the corresponding optimal encoding map. The process is iterative, with the channel fidelity increasing at each step until the value converges. To make the results sufficiently close to the optimal values, we randomly selected 20 initial encoding maps, iterated 2000 times and selected the highest value among them at each wait time t.

In the first part, we consider amplitude damping noise of the same intensity setting. Then, we consider a noise setting with different intensities for each qubit and simulate our algorithm by modifying the five-qubit $[[5,1,3]]$ code to adapt the asymmetrical thermal relaxation process. The noise model is shown formally in the following.

1. Amplitude Damping Error

Amplitude damping is energy loss from a quantum system. Energy loss occurs when the computational basis state $|1\rangle$ (excited state) decays into the computational basis state $|0\rangle$ (ground state). The single-qubit amplitude damping channel $\mathcal{N}_s^{ad}$ is described by the following Kraus representation:

$$\mathcal{N}_s^{ad}(\rho) = \sum_{k=0,1} E_k \rho E_k^{\dagger},$$

$$E_0 = \begin{bmatrix} 1 & 0 \\ 0 & \sqrt{1-\gamma} \end{bmatrix} \quad E_1 = \begin{bmatrix} 0 & \sqrt{\gamma} \\ 0 & 0 \end{bmatrix},$$

with $\gamma \in [0,1]$. We consider a quantum noise channel $\mathcal{N}$ that each qubit in the system suffers from the independent single-qubit amplitude damping noise with the same intensity.

2. Thermal relaxation process

A qubit can retain information for only a limited time called *Coherence Time*. There are two metrics to specify the coherence time of a quantum device. T_1 *Coherence Time* is associated with the energy loss that the excited state $|1\rangle$ naturally decays to the ground state $|0\rangle$. T_1 indicates the time for natural relaxation of a qubit. Besides this, qubits might interact with the environment and encounter a phase error, and the time constant associated with this error is called the T_2 *Coherence Time*.

The thermal relaxation process of a single qubit corresponding to wait time t can be described by the following map :

$$\rho = \begin{bmatrix} 1-\rho_{11} & \rho_{01} \\ \bar{\rho}_{01} & \rho_{11} \end{bmatrix} \longrightarrow \begin{bmatrix} 1-\rho_{11}e^{-\frac{t}{T_1}} & \rho_{01}e^{-\frac{t}{2T_1}-\frac{t}{T_\phi}} \\ \bar{\rho}_{01}e^{-\frac{t}{2T_1}-\frac{t}{T_\phi}} & \rho_{11}e^{-\frac{t}{T_1}} \end{bmatrix}, \tag{E1}$$

where $\frac{1}{T_\phi} = \frac{1}{T_2} - \frac{1}{2T_1}$ and $T_2 \leq 2T_1$. This process has the following Kraus representation:

$$\mathcal{N}(\rho) = \sum_{k=1,2,3} A_k \rho A_k^{\dagger},$$

$$A_1 = \begin{bmatrix} 1 & 0 \\ 0 & \sqrt{1-\gamma-\lambda} \end{bmatrix} A_2 = \begin{bmatrix} 0 & \sqrt{\gamma} \\ 0 & 0 \end{bmatrix} A_3 = \begin{bmatrix} 0 & 0 \\ 0 & \sqrt{\lambda} \end{bmatrix},$$

where $\gamma = 1 - e^{-\frac{t}{T_1}}$ and $\lambda = e^{-\frac{t}{T_1}} - e^{-\frac{t}{2T_2}}$. Such a CPTP map describes a Phase Amplitude Damping channel.